

Article

Digital Twin-Enabled Modelling of a Multivariable Temperature Uniformity Control System

Juan Gabriel Araque ¹, Luis Angel ¹ , Jairo Viola ^{2,*}  and Yangquan Chen ² 

¹ Electronic Engineering, Pontifical Bolivarian University, Medellin 050031, Colombia; araquemora@gmail.com (J.G.A.); luis.angel@upb.edu.co (L.A.)

² School of Engineering, University of California, Merced, CA 95343, USA; ychen53@ucmerced.edu

* Correspondence: jviola@ucmerced.edu

Abstract: The use of a digital twin as an enabling technology for industry 4.0 provides control systems engineers with novel tools for modelling, designing, and controlling complex systems, providing a deep understanding of the physical asset based not only on its physics but also the real system's response. It is particularly critical for uniformity temperature control applications, where providing a reasonable model of the system's diffusion is always affected by the physical behavior of the system's components required for heating, cooling, or power distribution. In this paper, a digital twin is used to represent a multivariable thermoelectric system employed for temperature uniformity distribution control with potential applications in semiconductor manufacturing. The modelling employs a five-step methodological framework consisting of the stages: target system definition, system description, multiphysics and data-driven simulation, behavioral matching, and implementation to represent the system's temperature distribution accurately. The temperature distribution is measured using an infrared thermal camera to perform model behavioral matching on heating and cooling temperature uniformity applications. The obtained results indicated that using digital twins not only increases the accuracy of the system's representation but can also provide the system with novel information that can be leveraged for the design and implementation of smart control systems.

Keywords: digital twin; behavioral matching; uniformity temperature modelling; sensitivity analysis



Citation: Araque, J.G.; Angel, L.; Viola, J.; Chen, Y. Digital Twin-Enabled Modelling of a Multivariable Temperature Uniformity Control System.

Electronics **2024**, *13*, 1419.

<https://doi.org/10.3390/electronics13081419>

Academic Editors: Sangchan Park, Sira Maliphol, Liu Fan and Jiyoung Woo

Received: 2 March 2024

Revised: 28 March 2024

Accepted: 7 April 2024

Published: 9 April 2024



Copyright: © 2024 by the authors. Licensee MDPI, Basel, Switzerland. This article is an open access article distributed under the terms and conditions of the Creative Commons Attribution (CC BY) license (<https://creativecommons.org/licenses/by/4.0/>).

1. Introduction

Uniformity temperature control is present in almost every manufacturing process, such as oil and gas, semiconductor, battery management, or steel casting, so accurate modelling of the system's thermal dynamics is crucial for the process analysis and controller design and implementation. For example, Ref. [1] presents the modelling and controls of the temperature distribution of a rotating cylinder surface using a tracking reference controller, which is designed using a finite elements approach by dividing the cylinder into several volumetric elements to define the correct electrode positions. Additionally, Ref. [2] shows the uniformity control of an industrial gas furnace for aluminum alloy manufacturing modelled based on the system partial differential equations and approached by a radial basis neural network to design a set of fuzzy PID regulators. Likewise, Ref. [3] expands the scope for the gas furnace by introducing optimal control rules to improve the temperature minimum margin on the system.

Moreover, temperature uniformity control plays a crucial role in the semiconductor manufacturing industry, considering that in a run-to-run and wafer-to-wafer execution of the system, the wafer temperature variability and its repeatability should be the same to keep stable conditions along the chip-making process. In Ref. [4], a thermal multizone approach is used to model a wafer heating process used in semiconductor lithography, which is used as a pseudo-inverse control approach to compensate for the air gaps on

the plasma. In addition, Ref. [5] proposes another spatial multi-heating zone approach to control uniformity temperature on a wafer, but it is based on a multi-level fuzzy logic. Likewise, Refs. [6,7] perform uniformity temperature control for lithography processes based on adaptive control or standard PI controllers based on reduced-order models of the wafer thermal behavior.

In that sense, this idea can be leveraged on different heating systems that use a thick metal plate to provide uniform surface heating or cooling. For example, Ref. [8] presents a temperature control mechanism based on moving plates to improve the performance of a thin surface plate. Likewise, Ref. [9] proposes a finite element grid modelling of an aluminum plate to develop a model predictive control method based on the average temperature control. In addition, in Ref. [10], a neural network-based controller is employed to regulate the temperature distribution on the hotplate of a power converter system. Furthermore, Ref. [11] presents a modelling method for piezoelectric heaters' temperature uniformity distribution based on single elements vibrations as heating energy sources. Notice that in the mentioned applications, the heating element employed corresponds to a semiconductor device (MOSFET), piezoelectric, or electrical resistor.

Another popular thermal application element is the Peltier thermoelectric device for heating and cooling conditions based on the current flow through the semiconductor material [12,13]. In that sense, there have been several applications where a Peltier cell, or an array of these, is employed for temperature uniformity control. For example, Ref. [14] presents the design of a 16 Peltier heating elements system for temperature uniformity control of a thin plate, modelled using a MIMO transfer function array and controlled using data-driven methods.

It is important to notice that the mentioned applications for temperature uniformity modelling and controls employ complex models to represent the system complexities like non-linearities, a multivariable nature, and the system's interaction with its environment. However, these models require a substantial computational load, a fine grid, finite element analysis methods, and temperature gradient considerations.

In that sense, a digital twin can be built based on some of the temperature modelling methods presented for temperature uniformity control applications with lower computational capability and reasonable accuracy. A digital twin can be defined as a virtual representation of physical assets that provides control systems designers with a high-fidelity model of a system that can be used not only for the design of advanced feedback control strategies but also to enable additional capabilities like fault detection, data analytics, or remaining useful life estimation [15–19]. Notice that the computational load of a virtual digital twin depends on the computational approach employed to represent the system (lumped elements, finite element analysis, partial differential equations, deep learning). As we emphasize in [19], a digital twin can be used as an enabling technology to provide awareness capabilities to a physical asset to develop smart control systems able to self-optimize with minimal user intervention to achieve a set of desired performance objectives based on analytics derived from the use of the digital twin like health prognosis, fault detection, or model predictive control.

However, the perspective about using a digital twin shown in [19] is focused on its implementation under an edge/embedded/hardware approach instead of a cloud solution. It means bringing the digital twin closer to the source of information to provide awareness capabilities to the system, leveraging the existing computational capabilities of processing systems installed on the physical assets without relying on additional cloud/enterprise solutions that could make the system sensitive to intellectual property violations or external attacks. In that sense, a digital twin should look to develop a physical asset representation that can be used as a reduced-order model (ROM) executable on embedded processors or the register transfer level (FPGA) to enable the development of smart controllers, bringing the process knowledge to the edge/embedded domain.

In this paper, a physics-based reduced-order digital twin model is developed to model a plate-based multivariable Peltier thermoelectric uniformity control system. The system

uses two Peltier heating elements to manage the temperature distribution on a planar copper plate. It uses an infrared thermal camera as a feedback sensor to capture the temperature distribution over the plate. The digital twin is modelled using the five-step design framework proposed by [20]. The physics-based model for the system is built in Matlab/Simscape R2022b. The Peltier thermoelectric heating elements are represented using the thermal and electrical properties. Likewise, the copper plate and its heat transfer properties are modelled using a discrete heat elements network representing the spatial conduction and convection heat transfer interactions between the plate, the Peltier heating sources, and the environment as shown in [21]. Thus, behavioral matching is performed to find the accurate values of the Peltier and thermal plate parameters, including heat capacities, thermal resistances (conduction and convection), copper coefficients, or Peltier thermoelectric parameters like the Seebeck coefficient, specific heats, and thermal masses, among others.

The behavioral matching employs real data from the infrared thermal camera corresponding to certain zones of the thermal plate that represent the temperature uniformity of the system. Likewise, a sensitivity analysis is performed via Monte Carlo simulation to determine the most influential parameters on the digital twin model, which can be used to design an awareness mechanism and control systems. The contributions of this manuscript are as follows:

- The development of a digital twin for multivariable temperature uniformity control systems based on Peltier thermoelectric heating elements using a discrete lumped elements approach and multiphysics behavior based on the DT development framework, which can be used for developing reduced-order models of the physical assets for its real-time execution on embedded devices.
- The use of the digital twin development framework to perform a series of behavioral matching algorithms to find the real values of the digital twin system's parameters using optimization tools.
- A sensitivity analysis is performed to determine the most influential parameters on the digital twin model based on its real behavior.

This paper is structured as follows. Section 2 briefly describes a digital twin and the five-step development framework. Section 3 shows the case study and the modelling employed for the digital twin. Section 4 presents the digital twin behavioral matching and sensitivity analysis. Finally, the Conclusions and Future Works are presented.

2. Digital Twin Development Framework

2.1. What Is a Digital Twin?

According to Refs. [22,23], a digital twin (DT) can be defined as a virtual representation of a physical system running alongside the real asset that reflects its behavior. A digital twin combines several representations to obtain the best system representation, including physics-based, data-driven, machine learning, or parametric models, among others [19,20]. Figure 1 represents a digital twin. It begins with a physical system comprising many different subsystems or elements that perform a specific task. The data streams from the physical system are sent in real time to the digital twin environment using the Internet of Things and edge computing devices. Inside the digital twin environment, a DT prototype describes the physical behavior of each component of the physical system and its interaction using multidomain physics tools and data-driven models incorporated in the digital twin environment. Thus, each DT instance sets a single representation of the physical system for a specific task, such as controller design, system component health, and prognosis.

It is important to notice that in Refs. [22,23], the replication of big physical assets inspires the target of digital twin applications and their conceptualization. Some examples include electric vehicle fleets, social behavior, climate change, and large manufacturing facilities. This is one of the most relevant applications for several industries on the path of DT adoption for digital transformation.

Therefore, from an industrial manufacturing point of view, digital twins can be analyzed on several levels, starting from subsystems and components, process replication, equipment modelling, shop floor simulation, manufacturing facility, and multi-factory simulation. Notice that most of the digital twin references and frameworks available in the literature are designed for their application at the shop floor level and above, the benefits of which are valuable from an enterprise and operational point of view. Due to the system's size and complexity, these approaches require more intensive utilization of breaking technologies like data analytics, artificial intelligence, or cloud computing.

However, similar ideas can be applied to the subsystem, process, and equipment modelling levels, which are the main target of this paper. According to Ref. [24], a digital twin can be differentiated from a pure simulation model in the sense that a physical asset must exist to be replicated into a virtual domain. Thus, the DT built for the uniformity temperature control system portrays the fundamentals of a digital twin.

Thus, the obtained DT model will be the starting point for the implementation of enabling technologies like fault detection, prognosis, or self-optimizing control methods. Likewise, the DT will be leveraged as a reduced-order model for its execution in embedded configurations, bringing the mentioned capabilities closer to the asset without additional hardware and communication infrastructure. A more detailed discussion regarding the digital twin concept and applications can be found in [19,20].

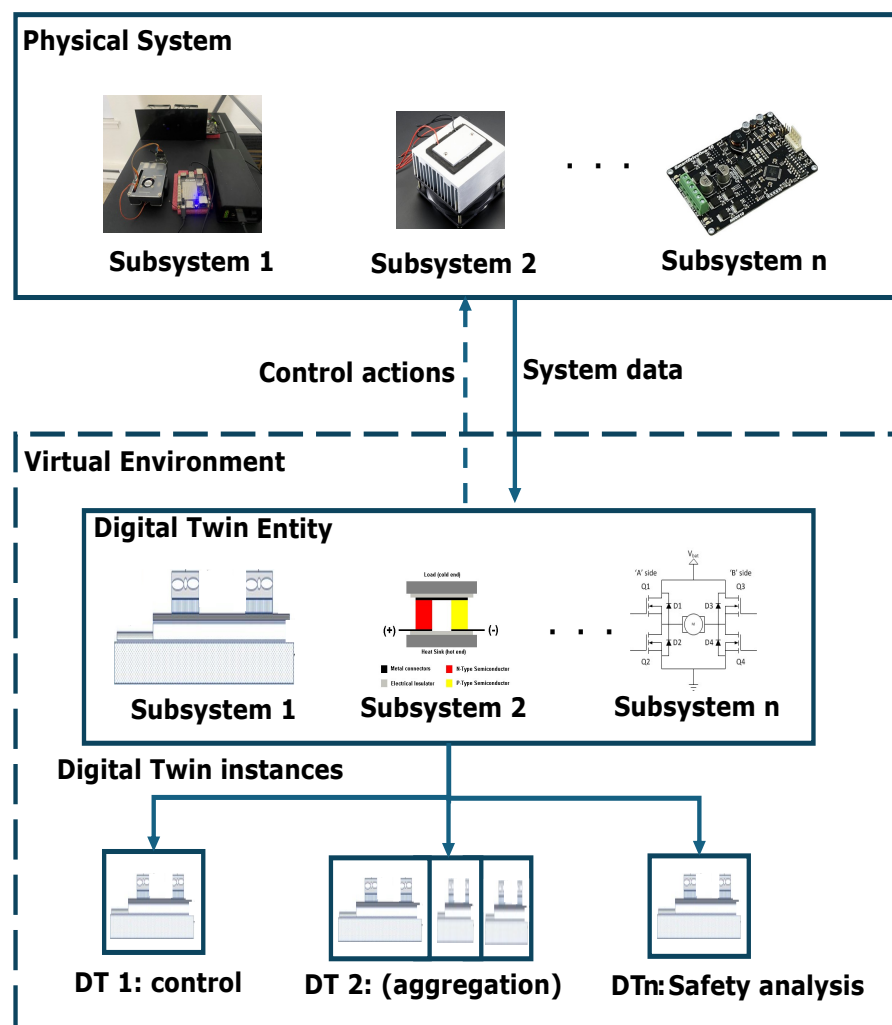


Figure 1. Digital twin conceptual diagram based on [19]. The physical asset domain shares the system's and subsystems' data with the virtual environment, where representations of each component are defined on a virtual prototype that can produce instances for different analysis and control tasks.

2.2. DT Development Framework

The DT methodological framework proposed by [19,20] shown in Figure 2 can be used to develop a digital twin application. It consists of five steps: target system definition, system documentation, multidomain simulation, DT behavioral matching, and DT evaluation and deployment. In the first step, target system definition, the physical asset is identified and assessed to establish its current status, operation mode, and feasibility for digital twin representation using CAD/CAM tools and physics-based and data-driven models. In the second step, system documentation, all the information related to the system, including existing manuals, blueprints, schematics, P&ID diagrams, datasheets, fault reports, and operation manuals, are collected to provide an in-depth understanding of the physical asset to replicate. Thus, the third step, multidomain simulation, consists of developing a comprehensive simulation model for the DT subsystems' dynamics based on multiphysics simulators like COMSOL, ANSYS, MSC-ADAMS, Matlab Simscape, among others, or data-driven methods like machine learning or reduced-order models. This model is validated based on the existing knowledge of the system. Once the DT is operative, the fourth step, behavioral matching, is performed, which consists of setting the DT within an optimization algorithm to match its operation with the physical asset using historical datasets, which allows for determination of the correct values of the system's parameters like frictions, stiffness, thermal capacitance, electrical inductance, sensor noise, among others. An extended discussion on DT behavioral matching for dynamical systems can be found in [25]. Finally, the fifth step, DT implementation and deployment, consists of delivering the model through user interfaces that enable the interaction between the users, the physical asset, and the DT. Depending on the system's complexity, it can be performed via edge computing with direct asset interaction or a cloud-based service if there are thousands of assets like a drone swarm or a fleet of autonomous vehicles. Each deployment can be used to monitor system faults, and enable awareness capabilities and remaining useful life prediction, among other functionalities.

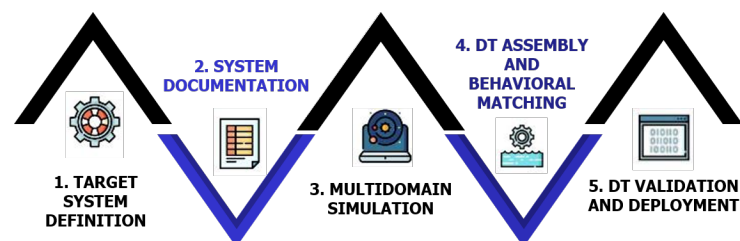


Figure 2. Digital twin five-step development framework.

3. Case Study: Uniformity Temperature Control Process Based on a Thermal Plate with Multiple Peltier Heating Elements

3.1. Steps 1 and 2: System Definition and Documentation

The multivariable temperature uniformity control system shown in Figure 3 is selected as a case study for its digital twin development and adjustment. The system is composed of four critical elements: a FLIR infrared thermal camera (B) and two Peltier thermoelectric modules (A1) and (A2) interconnected by a thin copper plate (A). The control unit is a LattePanda board (C) running Windows 10 and Matlab in a hardware-in-the-loop configuration (HIL) for manipulating Peltier cells and temperature readings from the thermal camera, which is communicated via TCP-IP. The dual power driver (D) controls the heating elements fed from a 12 V battery (E). Table 1 briefly summarizes the critical properties of the power driver, the Peltier modules, the infrared thermal camera, and the copper plate. The datasheet for the system's components can be found in [26–29]. A block diagram representation of the multivariable temperature uniformity control system is shown in Figure 4. The dual H-bridge manages the system's energy consumption via a PWM generator for each Peltier cell. Thus, the thermoelectric circuit of each Peltier device is connected to the

thermal distributed circuit corresponding to the metal plate, whose temperature is read by the thermal camera and sent to the LattePanda Board for data acquisition.

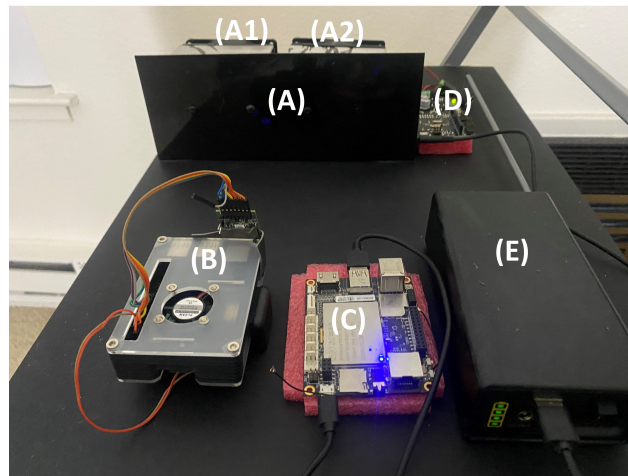


Figure 3. Case study: dual Peltier system with copper thin plate heating surface for temperature uniformity control applications. The system is composed of a thin copper plate (A) coupled with two Peltier thermal cells (A1), (A2) controlled using the power driver (D) with the energy provided by the battery (E). The LattePanda Computer (C) performs the temperature uniformity control using the infrared thermal camera (B) as feedback sensor.

Table 1. Multivariable Peltier thermal system documentation.

Component	Features
FLIR Lepton Thread Infrared Thermal Camera	Wavelength: 8 to 14 μm Resolution: 80×60 pixels Accuracy: ± 0.5 $^{\circ}\text{C}$
TEC1-12706 Peltier Module	$Q_{max} = 50$ W $\Delta T_{max} = 75$ $^{\circ}\text{C}$ $I_{Max} = 6.4$ A $V_{max} = 16.4$ V
URC10 Dual Output Power Driver	Input: 0–5 V Output: 8–25 V Peak Current: 30 A Built-in Arduino Uno
LattePanda board	5 inch Windows 1064 bits PC Intel Atom μp 4 GB of RAM
Thin Copper Plate	Size: $25 \times 10 \times 0.1$ cm (length, height, width) Specific heat 390 Jkg $^{-1}$ K $^{-1}$

The temperature uniformity distribution response of the system is shown in Figure 5 for different time instants: (a) 100 s, (b) 300 s, and (c) 500 s when a 50% duty cycle is applied to each cell. As can be observed, the dual Peltier cells heat the thermal plate, and it is noted that one of the cells has a stronger thermal interaction with the plate. This is caused by the mechanical attachment between the Peltier element and the copper plate, which is loose, producing a smaller thermal interaction. Likewise, notice that the infrared camera resolution of 80×60 pixels can provide a maximum of 4800 pixels with temperature measurements. Although this great feature provides superior sensing capabilities, it can make the digital twin computationally expensive for its evaluation and behavioral matching. For this reason, the thermal plate is divided into 12 heating zones and 3 central taps, as shown in Figure 5d for 15 temperature measurements. The first 12 correspond to the average temperature at each heating zone $T_{11} - T_{16}$ or $T_{21} - T_{26}$. The remaining parameters

correspond to the center taps T_{AM} , T_{BM} , and T_{CM} for the zones (A), (B), and (C), which provide information regarding the plate and Peltier heaters' interaction. The temperature response of each thermal zone T_{11} to T_{26} for 50% and 75% duty cycle inputs applied to the Peltier cells is shown in Figure 6. It can be observed that there is a difference in the maximum and minimum temperatures as shown in the thermal image.

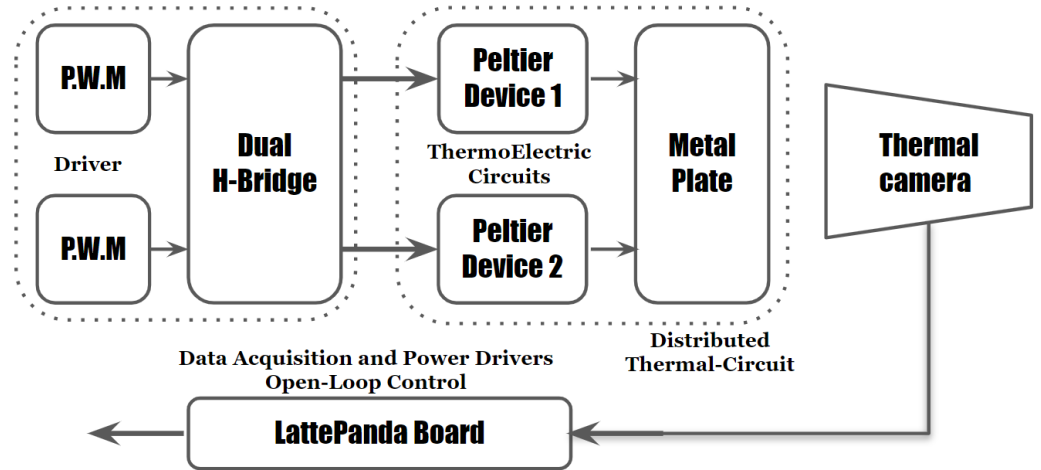


Figure 4. Block diagram of the multivariable Peltier uniformity temperature control system.

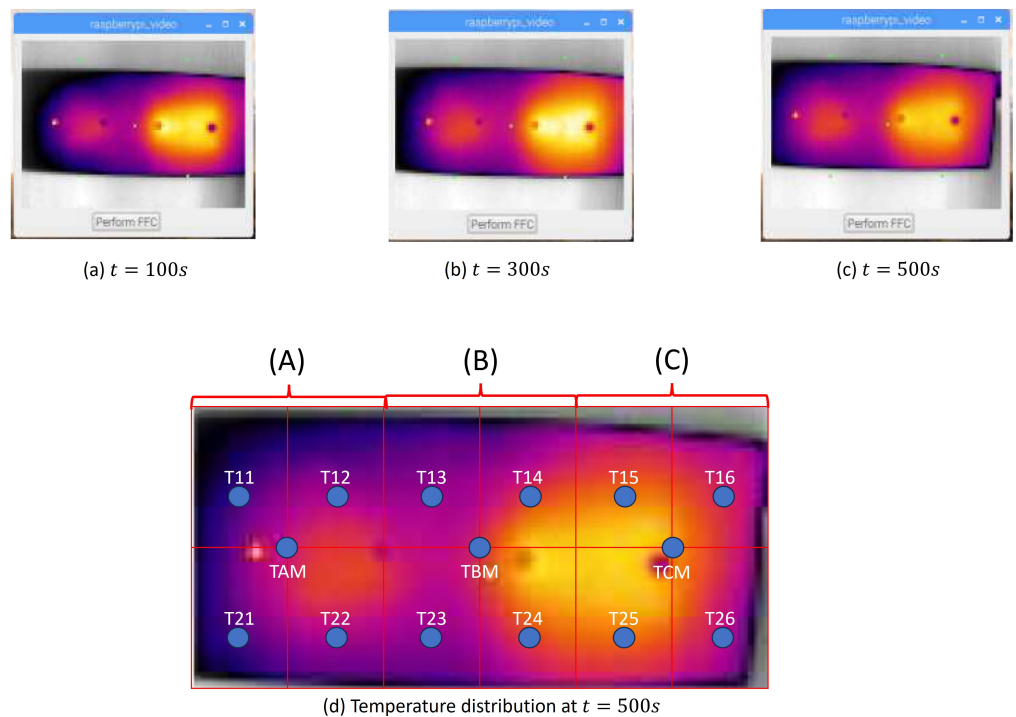


Figure 5. Uniformity temperature distribution acquired using the infrared thermal camera for the Peltier multivariable system. As can be observed, the copper plate heating process is performed for (a) 100 s, (b) 300 s, and (c) 500 s. The temperature measurements are distributed in three zones A, B, C divided as 2×6 grid as shown in (d), where the temperature where each partition is performed is the average temperature ($T_{11} - T_{16}$ and $T_{21} - T_{26}$) including the central tap measurements (T_{AM} , T_{BM} , and T_{CM}).

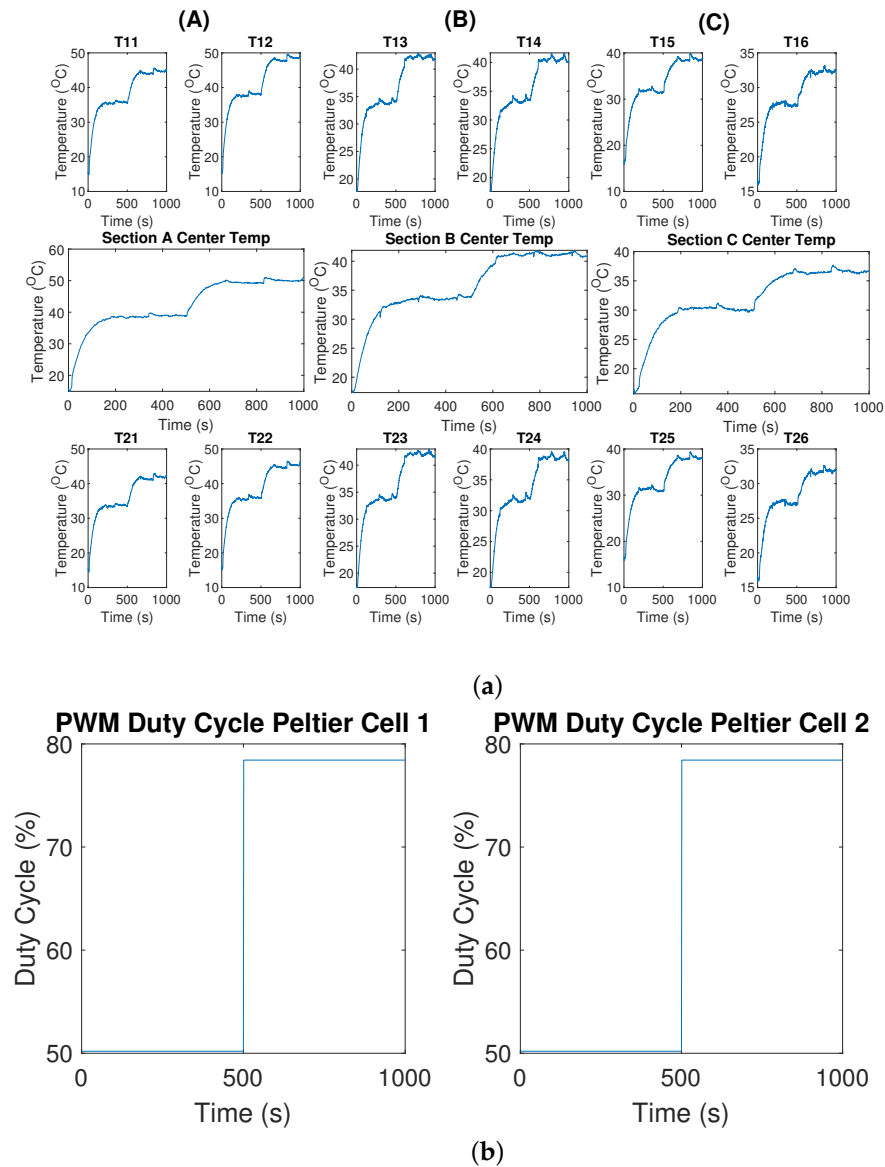


Figure 6. Temperature response for the copper plate measured temperature zones (a) $T_{11} - T_{16}$, $T_{21} - T_{26}$ and central taps for zones (A), (B), and (C) with the (b) PWM profiles of 50% and 78% for each Peltier element.

3.2. Step 3: DT Multidomain Simulation

This section’s goal is to model the multivariable thermoelectric process shown in Figure 3 and its thermal interactions using two thermally coupled equivalent circuits as shown in [21]. The first circuit corresponding to the Peltier element is built with discrete electrical and thermal components. It is coupled to the second circuit corresponding to the equivalent RC spatial network that models the heat transfer by conduction and convection through the copper plate to determine the spatial performance of the thermoelectric process. Its modular design makes it easier to add other thermal and electrical subsystems when it is necessary to change the operating conditions of the process.

3.2.1. Thermal Distributed Element Circuit

The thermal distributed circuit is shown in Figure 7 with the proposed volume elements’ V_{nm} distribution for the copper plate as shown in Figure 7a. The area of these elements is selected to be equal or proportional to the Peltier device area. This spatial coincidence makes it easier to connect the equivalent thermal circuits. Thus, the equivalent

circuit for heat transfer is based on the finite difference method and assumes that the temperature of each element of volume V_{nm} is spatially uniform at any instant during the transient process [30,31].

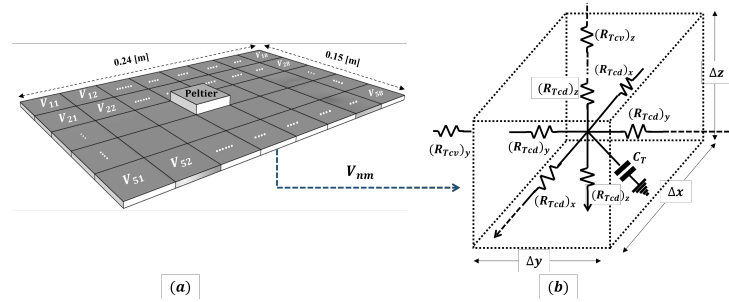


Figure 7. Thermal distributed element circuit: (a) copper plate volume elements’ spatial distribution where the Peltier heating device is fixed to one element and (b) the discrete thermal circuit for a single volume element.

On the other hand, Figure 7b, shows the thermal circuit of one volume element where C_T is the thermal capacitance representing the storage energy rate in a small volume of solid [32]. The conduction heat transfer resistance is modelled with the six thermal resistances oriented from the center of the volume element [33,34]. The other two resistors are used to model the convective heat flow between the metal surface and the environment. In a volume element, the energy storage change ΔU in a time interval Δt is expressed by (1), where m is the mass of the solid and c the specific heat, which is a thermal property of the material. C_T is defined as the thermal capacitance of the material.

$$\frac{\Delta U}{\Delta t} = mc \frac{\Delta T}{\Delta t} = C_T \frac{\Delta T}{\Delta t}, \quad \text{Then} \quad C_T = mc. \tag{1}$$

According to Fourier’s law for a solid [32], the heat transferred by conduction ΔQ in a time interval Δt is given by (2) where A is the cross-sectional area of the volume of element. Δl is the distance between the two ends at temperatures T_1 and T_2 . k is a proportionality constant called the thermal conductivity, which is a property of the material. R_{Tcd} is the material’s thermal resistance to the heat transfer by conduction.

$$\frac{\Delta Q}{\Delta t} = -kA \frac{T_1 - T_2}{\Delta l} = \frac{T_1 - T_2}{R_{Tcd}} \quad \text{Then} \quad R_{Tcd} = \frac{\Delta l}{KA}. \tag{2}$$

From (2), the six 3D-oriented thermal resistor of Figure 7b can be calculated by [33]:

$$R_{Tcdx} = \frac{\Delta x}{2K\Delta y\Delta z} \quad R_{Tcdy} = \frac{\Delta y}{2K\Delta x\Delta z} \quad R_{Tcdz} = \frac{\Delta z}{2K\Delta x\Delta y}. \tag{3}$$

Likewise, in the equivalent circuit shown in Figure 7b, R_{Tcv} is the thermal resistance to convective heat transfer between the surface of the volume element and a fluid around. According to Newton’s cooling law [32], when a solid is in thermal contact with a fluid, the convection heat ΔQ transferred in a time interval Δt is (4) where A and T_s are the area and temperature of the surface of the solid in contact with the fluid, T_∞ is the temperature of the fluid far from the surface, h is the convection transfer coefficient property of the fluid, and R_{Tcv} is the resistance to heat flow between the surface and the fluid.

$$\frac{\Delta Q}{\Delta t} = hA(T_s - T_\infty) = \frac{(T_s - T_\infty)}{R_{Tcv}} \quad \text{Then} \quad R_{Tcv} = \frac{1}{hA}. \tag{4}$$

The thermal equivalent circuit implemented in Simulink/Simscape for the copper plate is shown in Figure 8. The serial connection between the resistors of the volume elements allows for a reduction in the number of components in the circuit. The equivalent resistances R_{Tfx} and R_{Tcy} (5) are the serial sum of two adjacent resistors in the x - and y -axis, respectively. Likewise,

in Figure 8, R_{Tex} , R_{Tey} , and R_{Tez} given by (6) are the serial sum of the resistances to heat transfer by convection and conduction in the three-dimensional space, which is perpendicular to each of the environment contact surfaces. Finally, the thermal capacitances C_{Tnm} of the volume elements serve as a spatial reference. In Figure 8, the equivalent circuit nodes of each volume element can be used as measuring points of the temperature on the metal plate.

$$R_{Tfx} = 2R_{Tcdx} \quad \& \quad R_{Tcy} = 2R_{Tcdy}, \tag{5}$$

$$R_{Tex} = R_{Tcdx} + R_{Tcvx}; \quad R_{Tey} = R_{Tcdy} + R_{Tcvy}; \quad R_{Tez} = R_{Tcdz} + R_{Tcvz}. \tag{6}$$

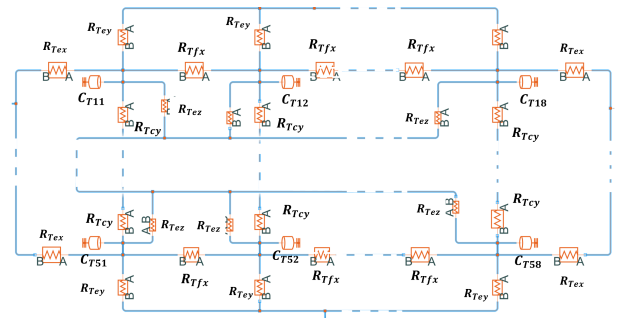


Figure 8. Simscape/Simulink model conductive and convective heat transfer equivalent on the plate.

3.2.2. Peltier Thermoelectrical Equivalent Circuit

The thermoelectric simulation circuit of Figure 9b was built based on the circuit of Figure 9a and [30]. This circuit includes the thermoelectric effects of Seebeck, Joule, and Peltier and the conduction heat transfer between the two sides of the device. In this case, the Peltier device transforms thermal energy into electrical energy by the Seebeck effect. The Electromotive Force $E.M.F(V)$ is given by (7) where α , T_h , and T_c are the Seebeck coefficient and temperatures on the cold and hot sides of the Peltier.

$$EMF = \alpha(T_h - T_c). \tag{7}$$

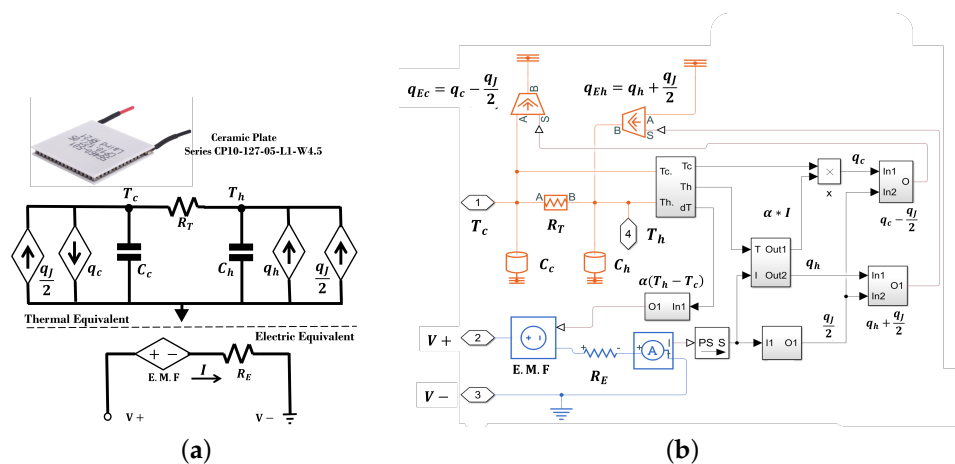


Figure 9. Case study: Peltier thermoelectrical equivalent circuit. (a) Theoretical model (in a similar manner as described by the study in [30]); (b) simulation model in Matlab/Simulink. The elements in blue are electrical, and those in orange are thermal.

Figure 9a shows the EMF implemented like an electric voltage-dependent source that depends on the temperature difference between the cold and hot sides. For the Joule effect, the heat rate q_J generated by the electrical current I through the electrical resistance R_E of the devices is given by (8).

$$q_J = I^2 R_E. \tag{8}$$

In the same way, Figure 9a shows how, in the thermal domain of the circuit, the Joule effect in (8) is divided into two dependent heat flow sources $\frac{q_J}{2}$, connected to the hot and cold nodes, respectively. Finally, the device transforms electrical energy into thermal energy by the Peltier effect. The heat rate dissipated q_c and absorbed q_h on the hot and cold side is calculated by (9) where π and α are the Peltier and Seebeck coefficients, T_c and T_h are the temperatures on the cold and hot sides of the Peltier device, and I is the electric current that flows through the device.

$$q_c = \pi I = \alpha T_c I \quad q_h = \pi I = \alpha T_h I. \tag{9}$$

The Peltier equivalent circuit is implemented in Simulink/Simscape using discrete thermal and electrical components as shown in Figure 9b. The heat flow sources in the Peltier device are modelled with two dependent heat flow sources q_{Ec} and q_{Eh} . These sources integrate both Joule q_J and Peltier ($q_c; q_h$) effects. The electrical and thermal input/output ports are depicted as $(V+, V-)$ and (T_h, T_c) . The heat capacity $c_{h,c}$ of C_h and C_c was calculated by equivalent thermal capacitance C_t taken from the study in Refs. [30,35], and the mass m of the device from the datasheets [36]. Likewise, according to [30], the Seebeck coefficient α , the electrical resistor R_E , and the thermal R_{Th} can be calculated using the manufacturer’s specifications [36] by substituting this device’s specifications into the equations below (10).

$$\alpha = \frac{V_{Max}}{T_h}; \quad R_E = \left(\frac{V_{Max}}{I_{Max}} \right) \left(\frac{T_h - \Delta T_{Max}}{T_h} \right); \quad R_{Th} = \left(\frac{\Delta T_{Max}}{I_{Max} V_{Max}} \right) \left(\frac{2T_h}{T_h - \Delta T_{Max}} \right). \tag{10}$$

The thermal and electrical performance of the Peltier circuit is evaluated using a DC Sweep analysis and compared to the manufacturer’s performance datasheet. The schematic for the DC Sweep analysis in the Peltier circuit operating in cooling mode is shown in Figure 10. The temperature source connected to the hot side of the Peltier circuit provides an ideal heat sink. The cold side is connected and the ideal load M_{load} is used to measure the heat absorbed. The DC sweep specifications are set on the *PWL* (Piecewise Lookup Current) source connected to the electric circuit input.

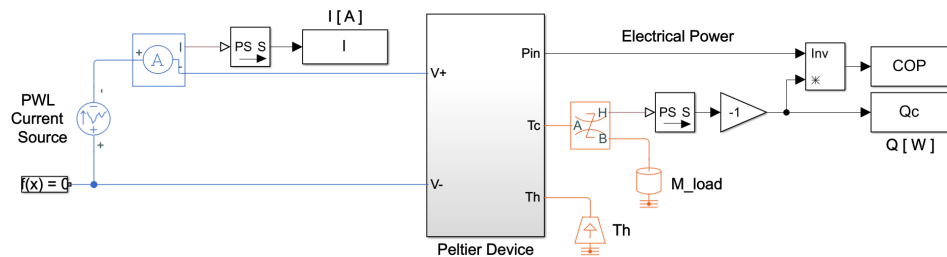


Figure 10. DC Sweep Simulink schematic for Peltier equivalent circuit performance.

Thus, the heat capacity $c_{h,c}$ was calculated with (10) and the equivalent thermal capacitance C_t estimated from the study in [30,35]. Using the values from Table 2 in (10), we can obtain the Seebeck coefficient and the electrical and thermal resistances listed in Table 3. The parameters used in the simulation are extracted from manufacturer datasheet CCP10-127-05-L1-W4.5 and given in Table 2 [36].

Table 2. Peltier specifications CP10-127-05-L1-W4.5 [36].

Hot Side Temperature at $T_h = 300$ K		
Symbol	Description	Value
Q_{cMax}	Maximum amount of heat absorbed at a Certain Load Specification when $\Delta T = 0$ K	33 W
ΔT_{max}	Maximum temperature differential. This point occurs when $Q_c = 0$ W	345.5 K
I_{max}	DC current level which will produce the maximum possible ΔT	4 A
V_{max}	DC voltage which will deliver the maximum possible ΔT across the device	13.9 V
m	Mass of the Peltier devices	9×10^{-3} Kg

Table 3. Peltier simulation parameters.

Hot Side Temperature at $T_h = 300$ K		
Symbol	Description	Value
α	Seebeck coefficient	0.0421 V/K
R_E	Electrical resistance	2.65 Ω
R_{Th}	Thermal resistance	3.22 K/W
$C_{h,c}$	Thermal equivalent capacitances (hot and cold sides)	5.68 J/K

DC Sweep obtains the Peltier response with the hot side temperature set to 300 K, which is shown in Figure 11a,b where $Q_c - I$ and $COP - I$ are the output characteristics of Peltier that were obtained by setting the initial temperature of the thermal load according to the temperature difference. It means that if the temperature difference is 60 K, the initial temperature of the load is set at 240 K. Otherwise, if the temperature difference is 30 K, the initial temperature of the load is set at 270 K, etc. This specification provides the initial temperature required for DC Sweep and ensures a better match with the performance of the datasheet.

Figure 11a presents the heat flow rate absorbed at the cold side concerning the input current. Notice that when the input current increases, the heat absorbed on the cold side increases to a maximum value. This behavior takes place by increasing the Joule effect. Moreover, Figure 11b shows the performance as a function of current for different temperature differences. The device’s dependency on temperature differences can be observed with the same input current value; the COP value is smaller for larger temperature differences. It means that the heat absorbed on the cold side is lower.

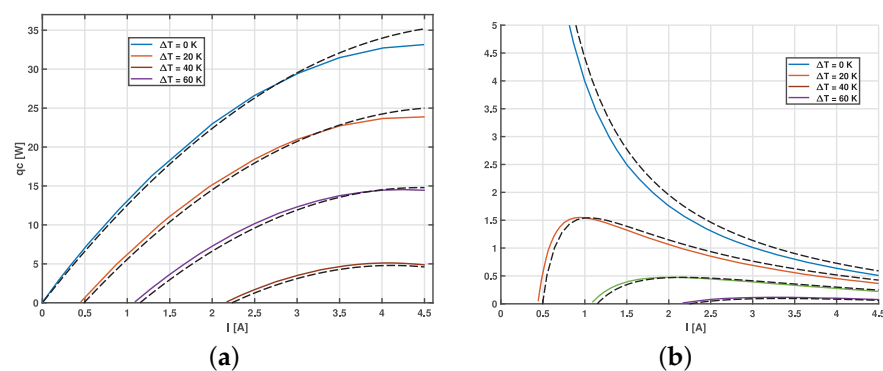


Figure 11. Peltier equivalent circuit performance. (a) Heat pumped on cold side $T_h = 300$ K. Dashed line, simulation circuit behavior. Solid line, graphic digitized from manufacture datasheet. (b) Coefficient of Performance ($COP = Q_c/P_{in}$) at $T_h = 300$ K. Dashed line, simulation circuit behavior. Solid line, graphic digitized from manufacture datasheet.

3.2.3. MIMO Digital Twin for the Uniformity Temperature Control System

The assembly of the digital twin for the multivariable temperature uniformity system presented in Figure 3 is composed of the Peltier thermoelectric circuit shown in Figure 9b and the thermal plate circuit for which the spatial volume elements' distribution is shown in Figure 12a. It consists of 24 individual volumes $V_{11} - V_{18}$, $V_{21} - V_{28}$, and $V_{31} - V_{38}$. Of these elements, 10 of them have dimensions of 4 cm \times 4 cm \times 0.1 cm (length, height, width), coinciding with the Peltier heating elements connected to the volume elements V_{23} and V_{26} . Additionally, with regard to the six elements representing the plate boundaries, V_{11} , V_{21} have dimensions of 1 cm \times 4 cm \times 0.1 cm, V_{31} has dimensions of 1 cm \times 3.5 cm \times 0.1 cm, V_{18} , V_{28} have dimensions of 1.5 cm \times 4 cm \times 0.1 cm, and V_{38} has dimensions of 1.5 cm \times 3.5 cm \times 0.1 cm. Likewise, the thermal distributed network circuit for the copper plate implemented in Simulink/Simscape is shown in Figure 12b. As can be observed, the 24 thermal elements' nodes are interconnected via discrete thermal resistors and capacitors as discussed in Figure 7b. The resistances on the top, bottom, left, and right sections of Figure 12b correspond to the heat transfer (conduction and convection) between the copper plate and the environment.

Thus, the fully assembled digital twin of the system is presented in Figure 13a. As can be observed, it is based on the thermal plate (distributed thermal circuit block) and the Peltier thermoelectric models (Peltier1 and Peltier 2 controller by a PWM input signal for each cell) provided in the previous sections.

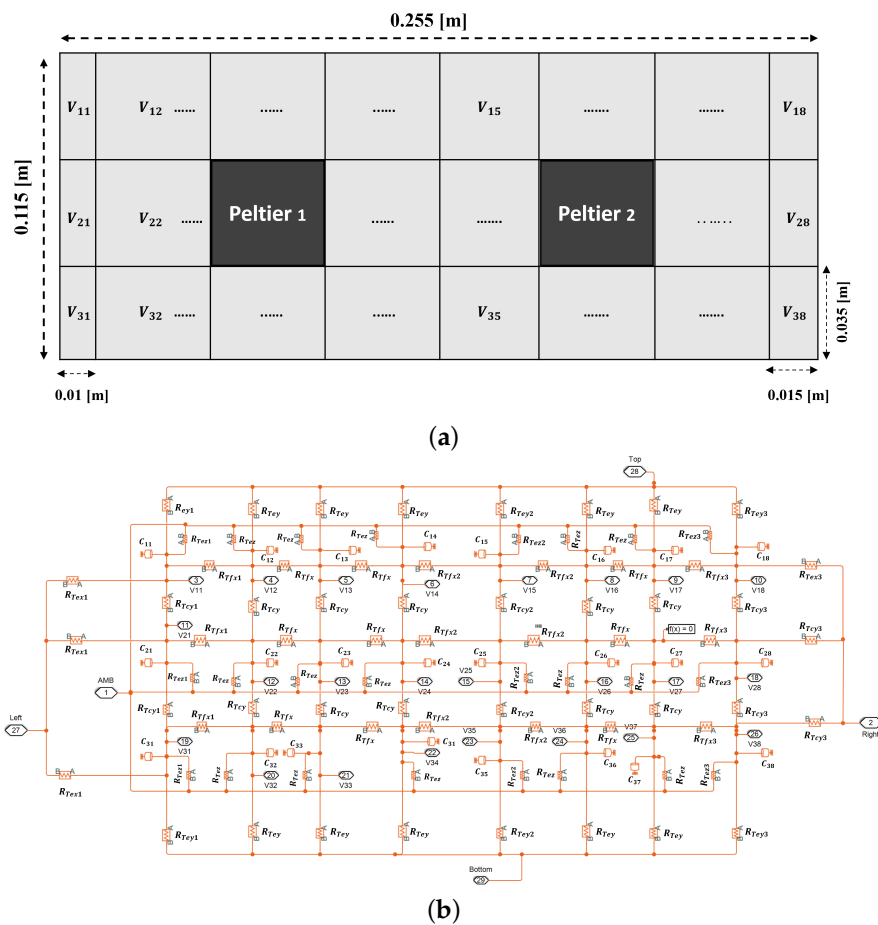


Figure 12. Spatial thermal plate volume elements distribution. (a) Thermal network for the copper plate with asymmetric volume elements on the left and right boundaries. (b) Simulink/Simscape model of the volumetric elements' interconnection based on discrete thermal elements (resistors and capacitors).

The thermal, electrical, and physical parameters employed on the digital twin are shown in Table 4, where C_{esp} is the copper-specific heat, R_{Th} and R_E are the thermal and electrical Peltier resistances, and the equivalent resistances R_{Tfx} and R_{Tcy} are the serial sum of two adjacent resistors in the x - and y -axis, respectively. The resistors (R_{Tex} , R_{Tey} , and R_{Tez}) are the serial sum of resistances to heat transfer by convection and conduction in the three-dimensional space. In the case of the thermal capacitances, $C_{Tnm} = 28.4$ J/K, and this is the same value for all the elements except for $C_{T11} = C_{T12} = C_{T13} = 7.1$ J/K, $C_{T15} = C_{T25} = C_{T35} = 21.3$ J/K, and $C_{T18} = C_{T28} = C_{T38} = 10.65$ J/K. The code for the MIMO Peltier digital twin and the datasets can be found in <https://github.com/tartanus/digital-twin-MIMO-peltier> (accessed on 30 March 2024).

The temperature uniformity of the system is shown in Figure 13b, where the two Peltier heaters working with a 50% duty cycle show a temperature gradient over the copper plate starting on the volume elements V_{23} and V_{26} . It shows the difference in the temperature distribution on the copper plate, which is caused by a loose mechanical and thermal coupling between one of the Peltier cells and the plate, which is accounted for during the parameter estimation process for the thermal elements associated with the volumetric elements V_{23} and V_{26} .

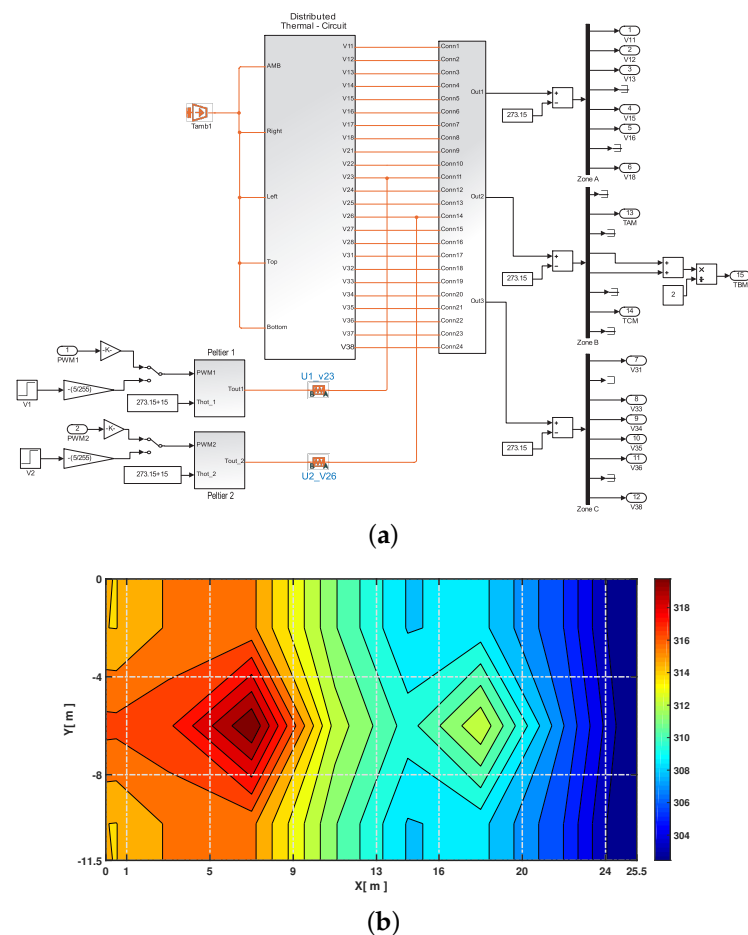


Figure 13. Consolidated MIMO digital twin for the uniformity temperature control system (a) Simulink/Simscape model with Peltier heating elements and the distributed thermal network for the copper plate. (b) Thermal uniformity distribution of the copper plate when a 50% duty cycle PWM signal is applied to the Peltier cells for heating applications.

3.3. Fourth Step: Digital Twin Behavioral Matching

The multiphysics model built in the previous section is intended to replicate the same behavior exhibited by the real system. In that sense, behavioral matching (BM) is required to match the digital twin response with the asset. The BM is performed through

an optimization process where the input/output data of the real system are compared with those from the digital twin. Thus, the quadratic error between the system’s response $\hat{y}(k)$ and its DT $y(k)$ (11) is used as a cost function to minimize the θ critical parameters on the model.

$$J_{bm}(\theta) = \frac{1}{N} \sum_{k=1}^N (y(k) - \hat{y}(k, \theta))^2. \tag{11}$$

For the proposed multivariable uniformity temperature application, several parameters influence the digital twin response matching, such as thermal resistances (conduction and convection) $R_{a1-3}, R_{xp1-3}, R_{yp1-3}$, specific heats C_{esp} , or thermal masses Q_s , which are defined in the previous section and can be grouped as $\theta = [C_{esp}, R_{a1-3}, R_{xp1-3}, R_{yp1-3}, R_p, R_c, R_{ph}, R_E]$. Although these parameters can be calculated from the material’s thermal properties and the volume element’s physical distribution, these values will differ from the physical system. Thus, the behavioral matching can help to find the values corresponding to the physical system to match the response. The Simulink Design Optimization (SLDO) Toolbox [37] is used as an optimization tool to find the values of θ . The initial values of θ are set as shown in Table 4. Non-linear least squares is used as an optimization method with an error tolerance of 1×10^{-3} as stopping criteria.

Table 4. Behavioral matching parameter estimation results.

Name	Variable	Initial Value	Final Value	Min	Max	Units
Peltier-specific heat	C_{esp}	1200	1959	0	2000	[J/(kg·K)]
Peltier Thermal Resistance	R_{Th}	1.86	9.75	0	12	[K/W]
Peltier Electrical Resistance	R_E	1.96	0.01	0	10	[Ω]
Thermal resistance	R_{Tfx} and R_{Tcy}	0.49	0.20	0	2	[K/W]
Thermal resistance	R_{Tez}	24.5	18.54	0	36	[K/W]
Thermal resistance	R_{Tez1}	50	95.5	0	200	[K/W]
Thermal resistance	R_{Tez2}	16.6	0.52	0	32	[K/W]
Thermal resistance	R_{Tez3}	33.3	0.82	0	70	[K/W]
Thermal resistance	R_{Tey}	197	149.6	0	400	[K/W]
Thermal resistance	R_{Tex1}	196.91	199.5	0	400	[K/W]
Thermal resistance	R_{Tex3}	196.94	16.11	0	400	[K/W]
Thermal resistance	R_{Tey1}	788.3	3.9	0	2000	[K/W]
Thermal resistance	R_{Tey2}	262.7	367.9	0	200	[K/W]
Thermal resistance	R_{Tey3}	545.5	315.5	0	200	[K/W]
Thermal resistance	R_{ph}	0.6	6.9×10^{-5}	0	2	[K/W]
Thermal resistance	R_{pc}	0.3	1.1	0	2	[K/W]
Thermal resistance	R_{Tfx2}	0.42	0.2	0	2	[K/W]
Copper-specific heat	C_{co}	196.94	16.11	0	400	[J/(kg·K)]

The behavioral matching results using the SLDO are shown in Figure 14 and in the fourth column of Table 4. It uses the input/output data shown in Figure 6 with 50% and 75% duty cycles for both Peltier heating elements for 500 s each. Each parameter is constrained based on its physical limitations. Likewise, the response of the digital twin against the physical asset is shown in Figure 15. For the 12 heating zones evaluated, it can be observed that the simulated response provided by the digital twin provides an accurate representation of the thermal plate temperature distribution. Although there are some cases like T16 or T31 where there is a small mismatching on some of the steady states, the transient response of the digital twin corresponds to the system’s physical behavior.

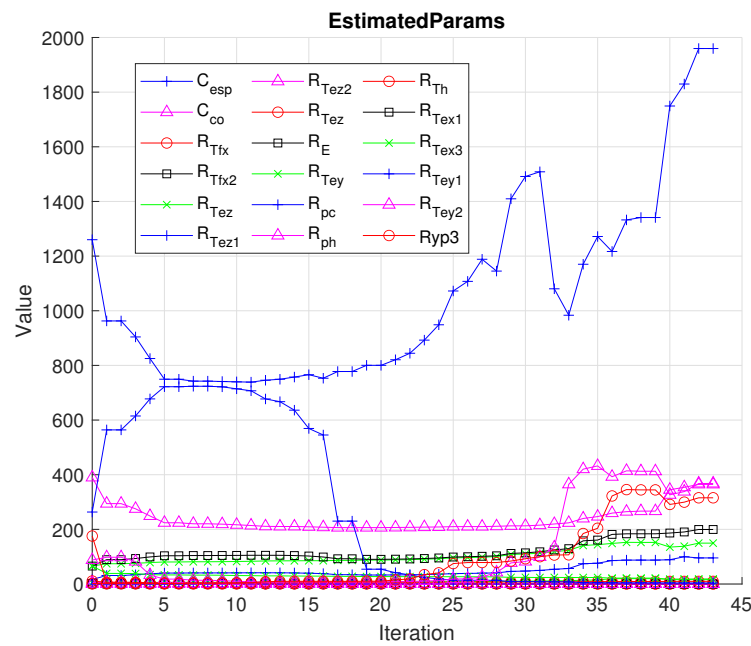


Figure 14. Digital twin behavioral matching results. The parameter optimization algorithm search for the correct values for the model parameters to match the digital twin with the real data acquired from the physical system.

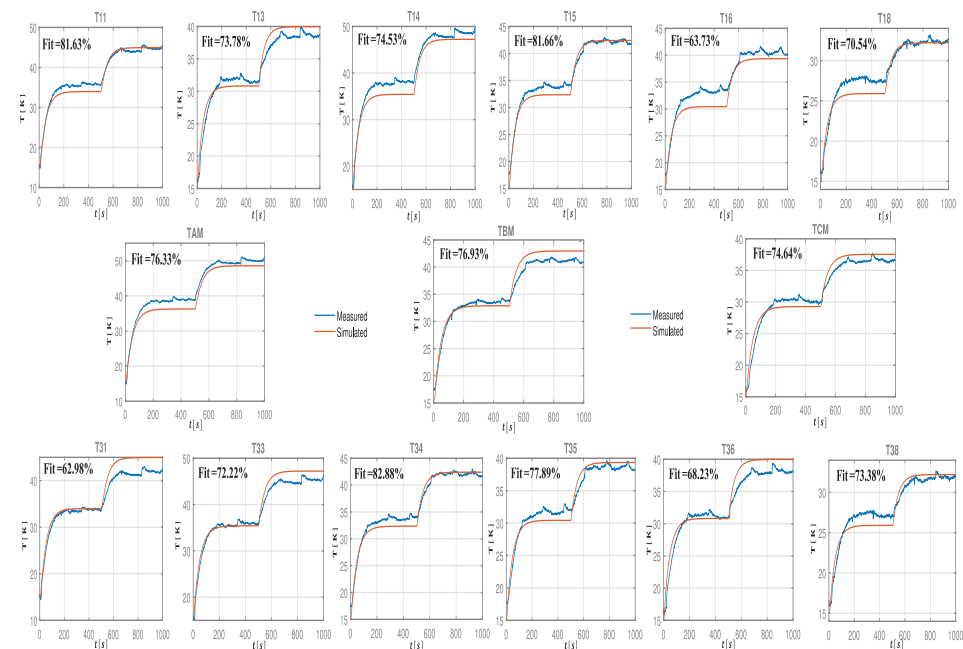


Figure 15. Digital twin’s adjusted response (red line) after behavioral matching process for the 12 thermal zones and central taps. The parametric adjustment process shows that the digital twin’s response is closer to the physical asset providing an accurate representation of the temperature distribution on the plate.

3.4. Sensitivity Analysis

According to [38], a sensitivity analysis is employed to evaluate the influence of model parameter errors on model results. It means quantifying how much the uncertainty in the system’s parameters and inputs modifies the system’s outputs. It can be performed in a local or total setup. A local sensitivity analysis, also called a variation method, only examines the influence of the change of one parameter on the simulated results. On the

other hand, a total sensitivity analysis examines the integrated influence of the change of several parameters on the simulated results and the interaction among model parameters based on simulation results. This technique has several applications, including oil and gas, water management, or social sciences [39–41]. In the case of the digital twin, there are some works where sensitivity analysis is used to analyze the performance of solar dryers [42], biogas facilities [43], or battery management, where statistical indices like the Pearson correlation is computed between the estimated and simulated performance indices of a battery [44].

This paper performs a post-optimization local sensitivity analysis to quantify the robustness of the cost function (11), corresponding to the model fit given by the quadratic error in the presence of parameter uncertainty. This analysis is performed using a Monte Carlo-like simulation. A set of normal distributions for each one of the digital twin parameters shown in Table 4 are generated using as the mean the values resulting from the optimization with a $\pm 25\%$ variance. A uniformly sampled population of 50 candidate solutions $\hat{\theta}$ were generated from the normal distributions and were evaluated on the digital twin model. As the sensitivity index, the Pearson correlation computed for the 12 heating zones and the central taps was selected. The resulting sorted correlation of the candidate solutions is shown in Figure 16. As can be observed for most of the zones, the resistance values for the interaction between the cell and the plate R_{pc} , and the Peltier electrical and thermal R_e and R_{Th} resistances show the strongest correlation regarding all the measured outputs of each volume element. In the case of extreme volume elements like T_{11} , T_{21} , the resistance R_{pc} exhibits a negative correlation; they indicate an inverse relation between the volume element temperature and that parameter. Likewise, the parameters R_a , R_p , R_{Te2} , as well as the specific heat C_{co} , exhibit almost no correlation (value close to zero) between the fitness of the model and the temperature response. In addition, an intermediate level of sensitivity is produced by the conduction and convection resistances along the copper plate edges, which is mostly negative, indicating that the effect on fitness is bigger as the values of the parameters are reduced. Thus, we can say that the Peltier electrical and thermal parameters should be prioritized during the optimization and experimental validation stages, considering their significant influence over the digital twin response fitness, which can be crucial for the design of fault detection, prognosis, and closed-loop control strategies.

3.5. Result Discussion and Next Steps towards Digital Twin-Enabled Capabilities

The digital twin model built for this paper's uniformity temperature control system shows an average accuracy of 70% for representing the heat distribution and behavior along the thermal plate for each heat zone. It means that the digital twin can support the design of model predictive and optimal control strategies, as well as predictive maintenance and data analytics applications. However, there are some aspects of the current digital twin implementation that need to be addressed to make the digital twin a smart control system.

Initially, how often does the execution rate of the behavioral matching need to be executed to determine the most updated parameters of the model? It requires an awareness and monitoring mechanism that detects any significant change in the system's response. In that sense, using a self-optimizing control layer enables system awareness by performing online optimization of the system's parameters along with the system's execution and parallel instances of the system's digital twin to accelerate its convergence and ensure that unsafe or unstable conditions are tested on the virtual environment before a final update of the DT model. In [45,46], some applications of self-optimizing control are employed for control systems' parametric updating, which could be used also for the digital twin behavioral matching.

On the other hand, the concept of smart control engineering shown in [19] uses a digital twin as an enabling technology to create smart systems. It means using a DT next to the source of information running on embedded hardware, requiring a reduced-order model digital twin compatible with the available hardware. Thus, the digital twin model developed in this paper serves as a starting point for deriving reduced-order models

on a set of finite volume elements grids that represent the temperature dynamics on the plate and a thermoelectric circuit for the Peltier heating elements. Behavioral matching was performed to adjust the digital twin model's behavior to that of the physical asset by adjusting the system's parameters. This calibration results in a good representation of the temperature dynamics. It is important to note that although only certain parts of the visual feedback from the thermal camera were used for the behavioral matching, the convergence and computational execution time of the model is reasonable and can be used for embedded code generation executable on embedded systems. Likewise, the sensitivity analysis shows that the Peltier thermal and electrical properties, as well as the thermal resistances between the Peltier cells and the copper plate, have a strong impact on the adjustment of the system's response, indicating that these parameters should be prioritized on upcoming and more complex thermal systems with features like redundant thermal actuators or simultaneous systems' interaction. Thus, the digital twin for the multivariable uniformity temperature control system enables a better understanding of the physical asset's behavior, properties, and current status, which can be used to develop informed feedback control strategies based on the components' health and remaining useful life. In future works, extending the sensitivity analysis for customized cost functions, including closed-loop control performance and economic considerations like energy consumption or environmental awareness, is proposed to provide more insights about the physical system towards implementing smart and self-optimizing controllers.

Author Contributions: Conceptualization, J.G.A., L.A., J.V. and Y.C.; methodology, J.G.A. and L.A.; software, J.G.A. and L.A.; validation, J.G.A., L.A. and J.V.; formal analysis, L.A. and Y.C.; investigation, J.G.A. and L.A.; resources, J.G.A., L.A., J.V. and Y.C.; data curation, J.G.A., L.A. and J.V.; writing—original draft preparation, J.G.A., L.A. and J.V.; writing—review and editing, J.G.A., L.A., J.V. and Y.C.; visualization, J.G.A. and L.A.; supervision, L.A. and Y.C.; project administration, L.A.; funding acquisition, L.A. All authors have read and agreed to the published version of the manuscript.

Funding: This research received no external funding.

Data Availability Statement: Data is contained within the article.

Conflicts of Interest: The authors declare no conflict of interest.

Abbreviations

BM	Behavioral Machine
CAD	Computer-Aided Design
CAM	Computer-Aided Manufacturing
COP	Coefficient of Performance
DT	Digital Twin
EMF	Electromotive Force
HIL	Hardware in the Loop
MIMO	Multiple Input Multiple Output
MOSFET	Metal Oxide Semiconductor Field Effect Transistor
PID	Proportional Integral Derivative
PWM	Pulse Width Modulation
SLDO	Simulink Design Optimization
TAM	Temperature Central Tap Heating Zone A
TBM	Temperature Central Tap Heating Zone B
TCM	Temperature Central Tap Heating Zone C
TCP-IP	Transmission Control Protocol/Internet Protocol

References

1. Fraczyk, A.; Kucharski, J. Surface temperature control of a rotating cylinder heated by moving inductors. *Appl. Therm. Eng.* **2017**, *125*, 767–779. [[CrossRef](#)]
2. Shen, L.; He, J.; Yang, C.; Gui, W.; Xu, H. Temperature Uniformity Control of Large-Scale Vertical Quench Furnaces for Aluminum Alloy Thermal Treatment. *IEEE Trans. Control Syst. Technol.* **2016**, *24*, 24–39. [[CrossRef](#)]

3. Shen, L.; Chen, Z.; Jiang, Z.; He, J.; Yang, C.; Gui, W. Optimal Temperature Rise Control for a Large-Scale Vertical Quench Furnace System. *IEEE Trans. Syst. Man Cybern. Syst.* **2022**, *52*, 4912–4924. [[CrossRef](#)]
4. Tay, A.; Ho, W.K.; Hu, N. An In Situ Approach to Real-Time Spatial Control of Steady-State Wafer Temperature during Thermal Processing in Microlithography. *IEEE Trans. Semicond. Manuf.* **2007**, *20*, 5–12. [[CrossRef](#)]
5. Zhang, X.X.; Li, H.X.; Wang, B.; Ma, S. A Hierarchical Intelligent Methodology for Spatiotemporal Control of Wafer Temperature in Rapid Thermal Processing. *IEEE Trans. Semicond. Manuf.* **2017**, *30*, 52–59. [[CrossRef](#)]
6. Tay, A.; Ho, W.K.; Wu, X. Real-Time Control of Photoresist Extinction Coefficient Uniformity in the Microlithography Process. *IEEE Trans. Control Syst. Technol.* **2007**, *15*, 99–105. [[CrossRef](#)]
7. Gumphier, J.; Bather, W.; Wedel, D. LPCVD silicon nitride uniformity improvement using adaptive real-time temperature control. *IEEE Trans. Semicond. Manuf.* **2003**, *16*, 26–35. [[CrossRef](#)]
8. Li, S.; Lou, G.; Wang, J. The temperature uniformity control of cooling system for medium plate. In Proceedings of the 2009 Chinese Control and Decision Conference, Guilin, China, 17–19 June 2009; pp. 3973–3975. [[CrossRef](#)]
9. Hosoya, N.; Yanou, A.; Minami, M.; Matsuno, T. A proposal of temperature control model for two dimensional aluminum plate using two degree-of-freedom generalized predictive control. In Proceedings of the 2014 SICE Annual Conference (SICE), Sapporo, Japan, 9–12 September 2014; pp. 1804–1809. [[CrossRef](#)]
10. Xu, S.; Shi, S.; Jiang, W.; Hashimoto, S. Cooperative Control of Recurrent Neural Network for PID-Based Single Phase Hotplate Temperature Control Systems. *IEEE Access* **2023**, *11*, 105557–105569. [[CrossRef](#)]
11. Chen, T.; Zhao, T.; He, Q.; Sun, R. Determination of vibration energy flow-controlling regions in a piezoelectric metamaterial plate with temperature rise. *Appl. Math. Model.* **2024**, *125*, 329–346. [[CrossRef](#)]
12. Mannella, G.A.; La Carrubba, V.; Brucato, V. Peltier cells as temperature control elements: Experimental characterization and modeling. *Appl. Therm. Eng.* **2014**, *63*, 234–245. [[CrossRef](#)]
13. Mironova, A.; Mercorelli, P.; Zedler, A. Chapter 3—Temperature control in Peltier cells comparing sliding mode control and PID controllers. In *Modeling, Identification, and Control for Cyber-Physical Systems towards Industry 4.0*; Mercorelli, P., Zhang, W., Nemati, H., Zhang, Y., Eds.; Emerging Methodologies and Applications in Modelling; Academic Press: Cambridge, MA, USA, 2024; pp. 41–77. [[CrossRef](#)]
14. Viola, J.; Rodriguez, C.; Chen, Y. PHELP: Pixel Heating Experiment Learning Platform for Education and Research on IAI-based Smart Control Engineering. In Proceedings of the 2020 2nd International Conference on Industrial Artificial Intelligence (IAI), IEEE, Shenyang, China, 23–25 October 2020; pp. 1–6.
15. Bobič, M. Digital Twin of Heat Exchanger. In *Heat Transfer*; Kazi, S.N., Ed.; IntechOpen: Rijeka, Croatia, 2022; Chapter 12. [[CrossRef](#)]
16. Xu, Z.; Xu, J.; Guo, Z.; Wang, H.; Sun, Z.; Mei, X. Design and Optimization of a Novel Microchannel Battery Thermal Management System Based on Digital Twin. *Energies* **2022**, *15*, 1421. [[CrossRef](#)]
17. Abdoune, F.; Nouiri, M.; Cardin, O.; Castagna, P. An enhanced methodology of Fault Detection and Diagnosis based on Digital Twin. *IFAC-PapersOnLine* **2022**, *55*, 43–48. [[CrossRef](#)]
18. Idrissi Kaitouni, S.; Ait Abdelmoula, I.; Es-sakali, N.; Mghazli, M.O.; Er-retby, H.; Zoubir, Z.; El Mansouri, F.; Ahachad, M.; Brigui, J. Implementing a Digital Twin-based fault detection and diagnosis approach for optimal operation and maintenance of urban distributed solar photovoltaics. *Renew. Energy Focus* **2024**, *48*, 100530. [[CrossRef](#)]
19. Viola, J.; Chen, Y. Smart Control Engineering Enabled by Digital Twin. In *Digital-Twin-Enabled Smart Control Engineering: A Framework and Case Studies*; Springer: Berlin/Heidelberg, Germany, 2023; pp. 73–102.
20. Viola, J.; Chen, Y. A Self Optimizing Control Framework and A Benchmark for Smart Process Control. In Proceedings of the 2021 3rd International Conference on Industrial Artificial Intelligence (IAI), Shenyang, China, 8–11 November 2021; pp. 1–6. [[CrossRef](#)]
21. Araque-Mora, J.; Angel, L. Distributed Equivalent Circuit for Modeling Heat Transfer Process in a Thermoelectric System. In Proceedings of the 2021 IEEE 5th Colombian Conference on Automatic Control (CCAC), Ibagué, Colombia, 19–22 October 2021; pp. 326–331. [[CrossRef](#)]
22. Grieves, M. Digital Twin: Manufacturing Excellence through Virtual Factory Replication. This Paper Introduces the Concept of a A Whitepaper by Dr. Michael Grieves. White Paper. 2014. Available online: <https://www.3ds.com/fileadmin/PRODUCTS-SERVICES/DELMIA/PDF/Whitepaper/DELMIA-APRISO-Digital-Twin-Whitepaper.pdf> (accessed on 1 January 2024).
23. Tao, F.; Qi, Q. Make more digital twins. *Nature* **2019**, *573*, 490–491. [[CrossRef](#)]
24. Wright, L.; Davidson, S. How to tell the difference between a model and a digital twin. *Adv. Model. Simul. Eng. Sci.* **2020**, *7*, 13. [[CrossRef](#)]
25. Viola, J.; Chen, Y.; Wang, J. Information-Based Model Discrimination for Digital Twin Behavioral Matching. In Proceedings of the 2020 2nd International Conference on Industrial Artificial Intelligence (IAI), Shenyang, China, 23–25 October 2020; pp. 1–6. [[CrossRef](#)]
26. Hebei I. T. (Shanghai) Co., Ltd. *Thermoelectric Cooler TEC1-12706*; Hebei I. T. (Shanghai) Co., Ltd.: Shanghai, China, 2010.
27. FLIR Systems Inc. *FLIR LEPTON® Engineering Datasheet*; FLIR Systems Inc.: Wilsonville, OR, USA, 2018.
28. LattePanda Inc.®. *LattePanda V1 Single Computer Board Datasheet*; LattePanda Inc.®: China, 2018. Available online: https://docs.lattepanda.com/content/1st_edition/power_on/ (accessed on 1 March 2024).
29. Cytron Technologies. *Sumo Robot Controller R1.1*; Cytron Technologies: Bukit Mertajam, Malaysia, 2024.

30. Lineykin, S.; Ben-Yaakov, S. Modeling and Analysis of Thermoelectric Modules. *IEEE Trans. Ind. Appl.* **2007**, *43*, 505–512. [[CrossRef](#)]
31. Astrain, D.; Vián, J.; Albizua, J. Computational model for refrigerators based on Peltier effect application. *Appl. Therm. Eng.* **2005**, *25*, 3149–3162. [[CrossRef](#)]
32. Incropera, F. *Fundamentals of Heat and Mass Transfer*; Wiley: New York, NY, USA, 2007.
33. Salome, P.; Leroux, C.; Crevel, P.; Chante, J.P. Investigations on the thermal behavior of interconnects under ESD transients using a simplified thermal RC network. *Microelectron. Reliab.* **1999**, *39*, 1579–1591. [[CrossRef](#)]
34. Lineykin, S.; Sitbon, M.; Kuperman, A. Spatial Equivalent Circuit Model for Simulation of On-Chip Thermoelectric Harvesters. *Micromachines* **2020**, *11*, 574. [[CrossRef](#)]
35. De Baetselier, E.; Goedertier, W.; De Mey, G. A survey of the thermal stability of an active heat sink. In Proceedings of the InterSociety Conference on Thermal Phenomena in Electronic Systems, I-THERM V, Orlando, FL, USA, 29 May–1 June 1996; pp. 373–382. [[CrossRef](#)]
36. Laird Thermal System. *Datasheet Ceramic Plate Series CP10-127-05-L1-W4.5*; Laird Thermal System: Morrisville, NC, USA, 2020.
37. Mathworks Inc. *Simulink Design Optimization*; Mathworks Inc.: Natick, MA, USA, 2020.
38. Zhao, C. Parameter sensitivity analysis of 3D numerical simulation in the high-pressure groundwater. In Proceedings of the 2011 International Symposium on Water Resource and Environmental Protection, Xi'an, China, 20–22 May 2011; Volume 1, pp. 157–160. [[CrossRef](#)]
39. Xue, L.; Xu, S.; Nie, J.; Qin, J.; Han, J.X.; Liu, Y.T.; Liao, Q.Z. An efficient data-driven global sensitivity analysis method of shale gas production through convolutional neural network. *Pet. Sci.* **2024**, *in press*. [[CrossRef](#)]
40. Rahmani, F.; Ataei, M.; Daghighi, S.M. Sensitivity analysis in quantitative modeling of toxicology. In *Encyclopedia of Toxicology*, 4th ed.; Wexler, P., Ed.; Academic Press: Oxford, UK, 2024; pp. 473–476. [[CrossRef](#)]
41. Tarantola, S.; Ferretti, F.; Lo Piano, S.; Kozlova, M.; Lachi, A.; Rosati, R.; Puy, A.; Roy, P.; Vannucci, G.; Kuc-Czarnecka, M.; et al. An annotated timeline of sensitivity analysis. *Environ. Model. Softw.* **2024**, *174*, 105977. [[CrossRef](#)]
42. Cetina-Quiñones, A.; Arici, M.; Cisneros-Villalobos, L.; Bassam, A. Digital twin model and global sensitivity analysis of an indirect type solar dryer with sensible heat storage material: An approach from exergy sustainability indicators under tropical climate conditions. *J. Energy Storage* **2023**, *58*, 106368. [[CrossRef](#)]
43. Pallavicini, J.; Fedeli, M.; Scolieri, G.D.; Tagliaferri, F.; Parolin, J.; Sironi, S.; Manenti, F. Digital twin-based optimization and demo-scale validation of absorption columns using sodium hydroxide/water mixtures for the purification of biogas streams subject to impurity fluctuations. *Renew. Energy* **2023**, *219*, 119466. [[CrossRef](#)]
44. Vandana.; Bose, B.; Garg, A. Sensitivity Analysis of Battery Digital Twin Design Variables Using Genetic Programming. In Proceedings of the 2023 IEEE 3rd International Conference on Sustainable Energy and Future Electric Transportation (SEFET), Bhubaneswar, India, 9–12 August 2023; pp. 1–6. [[CrossRef](#)]
45. Viola, J.; Chen, Y. An Accelerated Self Optimizing Control Framework for Smart Process Control Using Fractional Order Stochasticity. In Proceedings of the 2021 9th International Conference on Control, Mechatronics and Automation (ICCMA), Luxembourg, 11–14 November 2021; pp. 104–109. [[CrossRef](#)]
46. Viola, J.; Chen, Y. Parallel Enabled and Stability-Aware Self Optimizing Control with Globalized Constrained Nelder-Mead Optimization Algorithm. *IEEE J. Radio Freq. Identif.* **2023**, *7*, 178–181. [[CrossRef](#)]
47. Nwoke, J.; Milanese, M.; Viola, J.; Chen, Y.Q. FPGA-Based Digital Twin Implementation for Mechatronic System Monitoring. In Proceedings of the 2023 5th International Conference on Industrial Artificial Intelligence (IAI), Nianing, China, 21–24 August 2023; pp. 1–6. [[CrossRef](#)]
48. Nwoke, J.; Milanese, M.; Viola, J.; Chen, Y. FPGA-Based Digital Twin Implementation for Power Converter System Monitoring. In Proceedings of the 2023 IEEE 3rd International Conference on Digital Twins and Parallel Intelligence (DTPI), Orlando, FL, USA, 7–9 November 2023; pp. 1–6. [[CrossRef](#)]
49. Bouzid, S.; Viarouge, P.; Cros, J. Real-Time Digital Twin of a Wound Rotor Induction Machine Based on Finite Element Method. *Energies* **2020**, *13*, 5413. [[CrossRef](#)]
50. Dufour, C.; Soghomonian, Z.; Li, W. Hardware-in-the-Loop Testing of Modern On-Board Power Systems Using Digital Twins. In Proceedings of the 2018 International Symposium on Power Electronics, Electrical Drives, Automation and Motion (SPEEDAM), Amalfi, Italy, 20–22 June 2018; pp. 118–123. [[CrossRef](#)]

Disclaimer/Publisher's Note: The statements, opinions and data contained in all publications are solely those of the individual author(s) and contributor(s) and not of MDPI and/or the editor(s). MDPI and/or the editor(s) disclaim responsibility for any injury to people or property resulting from any ideas, methods, instructions or products referred to in the content.